Modelling radiation-induced oxidative dissolution of UO$_2$-based spent nuclear fuel on the basis of the hydroxyl radical mediated surface mechanism
Exploring the impact of surface reaction mechanism and spatial and temporal resolution

N.L. Hansson [a,*], M. Jonsson [b], C. Ekberg [a], K. Spahiu [a,c]

[a] *Nuclear Chemistry / Industrial Materials Recycling, Chalmers University of Technology, SE-412 96 Gothenburg, Sweden*
[b] *School of Engineering Sciences in Chemistry, Biotechnology and Health, Department of Chemistry, KTH Royal Institute of Technology, SE-100 44 Stockholm, Sweden*
[c] *Swedish Nuclear Fuel and Waste Management Co., SE-101 24 Stockholm, Sweden*

ARTICLE INFO

ABSTRACT

A combined kinetic and diffusion model with an accurate α-dose rate profile was used to model radiation induced dissolution of UO$_2$. Previous experimental data were used to fit the surface site reaction system involving the surface bound hydroxyl radical as an intermediate species for both UO$_2$ oxidation and surface catalysed decomposition of H$_2$O$_2$. The performance of the model was explored in terms of sensitivity to spatial and temporal resolution as well as simplifications in the models describing the surface reactions and the reactions in solution. As a result, optimal conditions for running the numerical simulations were identified.

© 2023 The Authors. Published by Elsevier B.V.
This is an open access article under the CC BY license (http://creativecommons.org/licenses/by/4.0/)

1. Introduction

The very high radiotoxicity and long half-life of the actinides in spent nuclear fuel require geological repositories for spent nuclear fuel that are based on combinations of barriers that can remain stable for extreme periods of time. In the event of groundwater intrusion due to multiple barrier failure, the spent nuclear fuel will be in contact with the groundwater. The strong radiation field originating from the fuel causes extensive water radiolysis, forming molecular and radical species which have a net kinetic oxidizing effect on the UO$_2$-matrix. The oxidation is mainly attributed to the molecular oxidant H$_2$O$_2$ [1,2]. As the UO$_2$ matrix is oxidized, the sparsely soluble U(IV) turns into the several orders of magnitude more soluble U(VI) [3], and thereby matrix dissolution with release of fission products as well as heavier actinides is enabled. Detailed knowledge about the mechanism and the kinetics of this process is of key-importance in the safety assessment of a geological repository. Given the extremely long time periods of relevance, mechanistic and kinetic data must be incorporated into numerical models allowing for long-term predictions.

A kinetic model describing radiation-induced dissolution of spent nuclear fuel must account for the radiation chemistry of the aqueous phase, the various reactions occurring at the interface between the fuel and the aqueous phase as well as diffusion in the system due to the concentration gradients evolving as a consequence of surface reactions and inhomogeneous distribution of the absorbed radiation. Furthermore, the model should be based on the input from a numerical model describing the geometrical dose distribution and the contribution of different types of radiation as well as being able to account for the impact of various solutes on the water chemistry as well as surface reactions. In many modelling-approaches, the geometrical dose distribution is treated using rough empirical estimations and approaches, such as the H$_2$O-UO$_2$ stopping power ratio method employed by Sunder et al. [4] which has been used in several previous studies [5–8]. A more rigorous dose rate model allows for the radiolytic production as a function of distance from the surface to be calculated, and not just at the liquid-surface interface [9–11]. Several groups have published studies of radiation-induced dissolution of spent nuclear fuel or model systems thereof that are based on numerical models [12–14]. Due to the complexity of the system, simplifications
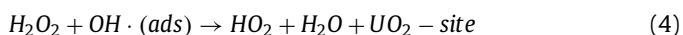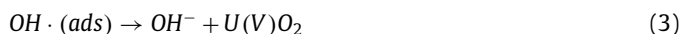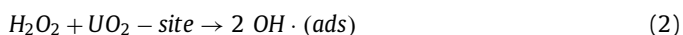
* Corresponding author.
  E-mail address: nikhans@chalmers.se (N.L. Hansson).

are often made in order to allow simulation over relevant time-periods. These simplifications may seriously influence the reliability of the models. Additionally, in groundwater, the ubiquitous carbonate species which can strongly complex and dissolve oxidized U(VI) from the UO_2 surface can have an important influence on the chemistry of the radiolytically produced oxidants.

Given the fact that the system of interest is characterized by continuous irradiation of the groundwater adjacent to the fuel surface at a dose rate that can be considered constant over fairly long periods of time, the most conservative approach that can be used is to assume that the rate of UO_2 oxidation and dissolution equals the rate of radiolytic oxidant production. This steady-state approach yields the maximum dissolution rate that can be attributed to water radiolysis. Since H_2O_2 has been found to be the radiolytic oxidant of main importance under the relevant conditions, the approach can be further simplified to include only H_2O_2 as the active UO_2 oxidant [15,16]. In its simplest form, the steady-state approach describes the kinetics of UO_2 dissolution in a system where H_2O_2 can only react with the surface and where reactions counteracting the oxidative dissolution can be neglected [17]. One of the main limitations with this approach is its inability to account for transients (i.e., changes in general conditions such as solutes and their concentrations). To achieve this, a model based on more complete mechanisms of the surface and solution reactions is required. Oxidation of UO_2 by H_2O_2 has often been described according to the following reaction:

$$UO_2 + H_2O_2 \rightarrow UO_2^{2+} + 2OH^- \tag{1}$$

with a second order rate constant reported as $k = 4.6 \cdot 10^{-6}$ m·min^{-1} at 1–100 mM HCO_3^- [18]. It has long been recognized that H_2O_2 can both oxidize the UO_2 surface and catalytically decompose to O_2 and H_2O on the same surface. To account for the competition between these two processes, the total rate constant for H_2O_2 consumption on the UO_2 surface has been expressed as the sum of the rate constants for oxidation and catalytic decomposition using a fixed ratio between the two [19]. However, this approach is not correct as demonstrated by the fairly recent works of Barreiro Fidalgo et al. [20] and Kumagai et al. [21]. These studies showed that the reaction order is not strictly one, even though the conditions in general would favour pseudo first order kinetics. The ratio between oxidation and catalytic decomposition was shown to be strongly dependant on the concentration of H_2O_2, and to some extent on the accumulated exposure. The reaction mechanism proposed to account for these observations is the one described in Eq. (2)-(5) [21,22].

$$H_2O_2 + UO_2 - site \rightarrow 2\ OH \cdot (ads) \tag{2}$$

$$OH \cdot (ads) \rightarrow OH^- + U(V)O_2 \tag{3}$$

$$H_2O_2 + OH \cdot (ads) \rightarrow HO_2 + H_2O + UO_2 - site \tag{4}$$

$$HO_2 + HO_2 \rightarrow H_2O_2 + O_2 \tag{5}$$

As can be seen, the oxidation and catalytic decomposition processes are intimately connected with a common intermediate, the surface bound hydroxyl radical. The catalytic decomposition mechanism has been confirmed for a number of other oxide surfaces (that cannot undergo further oxidation) and the overall mechanism accounts for the observed H_2O_2 concentration dependence. The involvement of the surface bound hydroxyl radical opens new possible reaction routes that cannot be accounted for by the more traditional description of the process. It has been shown in many studies that the surface bound hydroxyl radical can be scavenged by certain solutes, and this would indeed have an impact also on

the radiation induced dissolution of spent nuclear fuel. It is therefore essential to base future simulations of radiation induced dissolution of spent nuclear fuel on this mechanism. In addition to a more detailed mechanism of the surface reaction, the spatial and temporal resolutions of the numerical model are important parameters. The resolution becomes increasingly important in systems that have not reached steady-state or where the conditions are changing rapidly.

In this work we introduce a novel numerical modelling approach for radiation-induced oxidative dissolution of UO_2-based spent nuclear fuel accounting for the radiation chemistry of water with both spatial and temporal resolution, surface reactions and diffusion. The radiation chemistry simulations are based on calculated α-dose rate profiles. The influences of spatial and temporal resolution are investigated and the impact of the mechanism for H_2O_2 induced oxidation of UO_2 is quantified.

2. Method and models

2.1. Radiolysis

The dose rate profile is modelled through generation of α-particles within the UO_2-matrix which are stepwise attenuated based on stopping power data in the UO_2-matrix and adjacent water layer using a model developed previously by our group [10,11]. The dose rate and thereby also the radiolytic production is highest at the fuel surface, beyond which it trails off towards the maximum α-particle range in water of ~45 μm. Stopping powers were taken from the ASTAR database combined with the continuous slowing down approximation (CSDA) which deviates by just a few percent from the projected range algorithm (PRAL) integrated into the SRIM program [10]. The CSDA approach is conventionally used and is adopted in the current work. The radiolytic production perpendicular to the fuel surface has a resolution of 0.01 μm, allowing for a high resolution of the in-data to the coupled kinetics and diffusion model. This allows for reactions close to the fuel surface to be modelled accurately under short time scales, which would not be possible using a homogenized radiolytic production.

2.2. Kinetic model

The kinetic model includes a complete reaction scheme for the radiation chemistry of water including reactions involving bicarbonate/carbonate and surface reactions between H_2O_2 and UO_2. The rate constants were obtained from refs. [23–27]. (The full reaction set is shown in Table S1, supplementary material.) To account for the system heterogeneity, the water volume is divided into layers of equal thickness. The surface reactions only occur at the liquid-surface interface, i.e., in the first solution layer. The groundwater at a typical repository site is expected to have HCO_3^- concentrations of ~2 mM [28], which means that the carbonate concentration will be within the range for first order kinetics when describing the dissolution process according to the work of Hossain et al. [18]. The initial water composition in a general simulation of radiation induced dissolution of spent nuclear fuel consists of 10 mM total carbonate concentration, with H_2CO_3, HCO_3^- and CO_3^{2-} concentrations in equilibrium with respect to $pK_{a1}=6.35$ and $pK_{a2}=10.33$ [3,29].

Two different descriptions of the kinetic reaction scheme were adopted to describe reactions in solution, one including all reactions from the full reaction set (shown in Table S1, supplementary material), and one including no reactions in solution. Both of these reaction sets were combined with the surface reaction or reactions between UO_2 and H_2O_2. These two descriptions are labelled full and simplified reaction schemes. Therefore, in the simplified reac-

Table 1

G-values (molecules/100 eV) for the radiolytic species produced during water radiolysis [13].

Species	$G(H_2O_2)$	$G(OH\cdot)$	$G(OH^-)$	$G(e_{aq}^-)$	$G(H_2)$	$G(H\cdot)$	$G(H^+)$	$G(HO_2)$
α - 5 MeV	1.00	0.35	0.03	0.15	1.20	0.10	0.18	0.10
γ-rays	0.70	2.70	0.50	2.60	0.45	0.66	3.10	0.02

Table 2

Surface site reaction system.

$O_2 + UO_2 - site \rightarrow 2\ OH \cdot (ads)$	ks1
$OH \cdot (ads) \rightarrow OH^- + U(V)O_2$	ks2
$H_2O_2 + OH \cdot (ads) \rightarrow HO_2 + H_2O + UO_2 - site$	ks3
$HO_2 + HO_2 \rightarrow H_2O_2 + O_2$	ks4
$U(V)O_2 + U(V)O_2 \rightarrow U(VI)O_2(aq) + UO_2 - site$	ks5

tion scheme, only the reaction or reactions between UO_2 and H_2O_2 are considered.

As the model developed in this work is not based on the steady-state approach nor any other simplifying assumptions, it can be used to investigate the impact of individual processes on the system behaviour prior to reaching steady-state. The kinetic reaction system can be expressed in terms of mass balances of the involved species. This mass balance system is a system of ODEs which can be numerically solved using explicit or implicit ODE solvers. The large variation in the values of the rate constants puts additional constraints on the solver [30]. The mass balance reaction system is written in MATLAB 2019a and is solved using the ode15s solver, which is appropriate for the stiff system in which rate constants vary by several orders of magnitude [30,31]. The relative and absolute tolerance levels were chosen as 10^{-5} and 10^{-15} respectively, which gives a high degree of accuracy in the solver.

2.3. Escape yields

As the α-particle is attenuated, the LET-value changes, which in turn changes the radiolytic yields. In order to calculate the radiolytic yields of the attenuating α-particles with high precision, the G-values should be given as a function of the LET value. Additionally, G-values in the first monolayers of water at H_2O-oxide interfaces can be significantly altered as shown in the work of LaVerne and Tandon [32]. This should however not have a considerable effect in the systems modelled in this work, as the range of an α-particle is significantly larger than the size of a few water layers. In this work, the simplification that the G-values can be expressed by using the average LET-value for α-particles of a certain energy is therefore used. This approach is commonly adopted in combined radiolysis and kinetic models [13,33].

The radiation chemical yields after the nonhomogeneous regime, G-values, for all aqueous radiolysis products are taken from the work of Pastina and LaVerne and are shown in Table 1 (in units molecules/100 eV) [13]. The G-values in the work of Pastina and LaVerne were initially obtained by the authors from the references [34–40] and were then adjusted to improve the agreement between their experimental water decomposition product concentrations and their kinetic system based on the rate constants of refs. [23–26].

2.4. Surface site reaction system

The surface site reaction system is shown in Table 2. In the model, the surface adsorbed OH·-radicals only form in the reaction between H_2O_2 and the UO_2 sites. In general, hydroxyl radicals formed from radiolysis of water could also adsorb to the surface. However, this process is not accounted for in the present version of our model. As the rate constants for these reactions have not

been determined experimentally, previously published experimental data were used to determine the rate constants through a numerical fitting procedure. A surface site density of $2.1 \cdot 10^{-4}$ mol/m^2 was used in the model [18]. The MATLAB function lsqnonlin was used to minimize the residual of the modelled concentration profiles to the experimental H_2O_2 and U(VI)(aq) data by fitting the values of the constants ks1, ks2, ks3 and ks5 using the full reaction set to describe the solution chemistry. As ks4 has previously been determined [26], it was not fitted in this work. The residuals of the data sets were normalized with respect to their initial H_2O_2 concentration to normalize their weights in the fitting procedure.

2.5. Diffusion model

The diffusive transport was modelled using an implicit scheme to solve Fick's second law shown in Eq. (7):

$$\frac{\partial c}{\partial t} = D \frac{\partial^2 c}{\partial x^2} \tag{7}$$

The model is purely diffusion-controlled with convection set to zero. The implicit scheme is unconditionally stable and is based on evaluating the partial differential equation using a backward difference approximation of $\frac{\partial c}{\partial t}$ at $(i, j+1)$:

$$\left.\frac{\partial c}{\partial t}\right|_{i,j+1} = \frac{c_{i,j+1} - c_{i,j}}{\Delta t} \tag{8}$$

and a second order central difference approximation of $\frac{\partial^2 c}{\partial x^2}$ at $(i, j+1)$:

$$\left.\frac{\partial^2 c}{\partial x^2}\right|_{i,j+1} = \frac{c_{i+1,j+1} - 2c_{i,j+1} + c_{i-1,j+1}}{\Delta x^2} \tag{9}$$

where i is the spatial index, j is the temporal index, Δt and Δx are the temporal and spatial step sizes respectively. Inserting Eq. (8) and (9) into (7) gives:

$$c_{i-1,j+1} - \left(2 + \frac{\Delta x^2}{D\Delta t}\right)c_{i,j+1} + c_{i+1,j+1} = -\frac{\Delta x^2}{D\Delta t}c_{i,j} \tag{10}$$

with the unknowns: $c_{i-1,j+1}$, $c_{i,j+1}$ and $c_{i+1,j+1}$. This set of equations was implemented in MATLAB 2019a and expressed as a matrix system of n equations with one equation for each unknown value, as shown in Eq. (11) for the $n = 3$ case:

$$\begin{pmatrix} c_{1,2} \\ c_{2,2} \\ c_{3,2} \end{pmatrix} = \begin{pmatrix} 1+2\delta & -\delta & 0 \\ -\delta & 1+2\delta & -\delta \\ 0 & -\delta & 1+2\delta \end{pmatrix} \begin{pmatrix} c_{1,1} \\ c_{2,1} \\ c_{3,1} \end{pmatrix} + \vec{b} \tag{11}$$

where $\delta = \frac{\Delta x^2}{D\Delta t}$ and $\vec{b}$ is the boundary condition vector. The closed system was simulated using no flux Neumann boundary conditions at both the inner and outer boundary, meaning no species can leak out of or into the system, i.e., for the $n = 3$ system $\frac{\partial c_{0,1}}{\partial x} = 0$ and $\frac{\partial c_{4,1}}{\partial x} = 0$. Dirichlet boundary conditions, meaning a fixed concentration at the boundary, was also investigated in the benchmarking of the model. The matrix system was solved using an implicit solution method which is unconditionally stable with O(Δt) accuracy in time and O(Δx^2) accuracy in space. The unconditional stability means that an arbitrary time step can be employed without introducing instability in the mathematical solution.
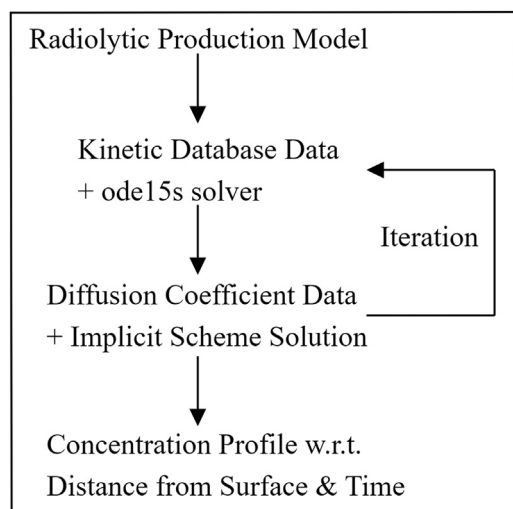
Fig. 1. Coupled kinetic- and diffusion model process flowsheet.

Table 3
Results from the homogeneous irradiated Fe^{2+}-Fe^{3+} system.

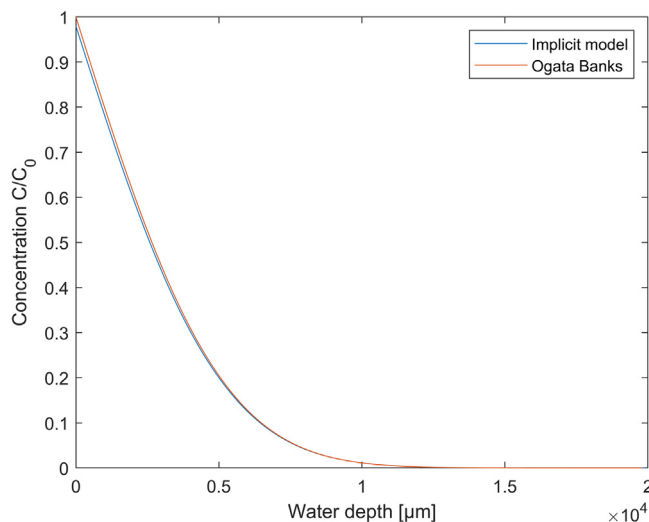| Water layer average dose rate [Gy/h]	$G(Fe^{3+})$ [molecules/eV]
$8.3 \cdot 10^{-6}$	0.0742
$8.3 \cdot 10^{-3}$	0.0742
8.3	0.0742
$8.3 \cdot 10^{3}$	0.0731
$8.3 \cdot 10^{6}$	0.0021

Fig. 2. Comparison between the implicit model and the analytical Ogata Banks solution to the Dirichlet boundary condition case in a 10^4 μm system with 100 layers modelled for 10^4 time steps of 0.36 s.

2.6. Integrated model description

Radiolytic production, kinetic and diffusion models are coupled in an iterative 1D-procedure using a unit fuel surface area. The species initially present, as well as those produced through radiolysis, react in the kinetic step before the species can diffuse between layers in the diffusion step. The diffused system is the in-data in the next time step in the kinetic simulation. Both the kinetic and diffusion steps are run for the same time step duration with a resolution of 50 computational steps within each time step. The simplified computational scheme is shown in Fig. 1. The model allows for the system to be divided into layers of arbitrary thickness and time into steps of arbitrary length. A rather low dose rate of 1 Gy/h was mainly studied in order to be able to compare the results of the steady-state approximation with the simplified and full reaction systems without the effect of e.g., a notable H_2 build up. The low dose rate was also used when investigating the influence of model parameters such as spatial and temporal resolution.

In the work of Poulesquen and Jégou, a similar iterative procedure was used, in which the set of kinetic equations was solved during a kinetic calculation step using Chemsimul, followed by a separate diffusion step using no flux Neumann boundary conditions [38]. Additionally, in the work of the authors, the radiolytic production from α-particles was modelled by considering the Bragg-peak nature of the stopping power spectrum, leading to a higher radiolytic production in the outer water layers of the irradiated 40 μm segment [38]. The influence of the dose rate profile was also considered in the present work.

3. Results and discussion

3.1. Benchmarking

3.1.1. Radiolysis and kinetic reaction system

To benchmark the MATLAB code and the reaction set used in the simulations, the model was used to simulate the Fricke dosimeter in a homogeneously γ-irradiated system [41]. The G-values used are shown in Table 1. Under deaerated conditions, $G(Fe^{3+})$ can be calculated as [42,43]:

$$G\left(Fe^{3+}\right) = 2G(H_2O_2) + G\left(e_{aq}^-\right) + G(\cdot H) + 3G(\cdot HO_2) + G(\cdot OH)$$
$$= 0.0742 \; molecules/eV \quad (12)$$

The Fricke dosimeter utilizes acidic conditions, under which Fe^{3+} is stable. In the modelled system, the pH is set to 0, suffi-

ciently acidic to prevent precipitation of Fe^{3+}. The initial Fe^{2+} concentration was 0.5 M, to ensure that the G-value is independent of the concentration. This is especially relevant under high dose rates. The kinetic reaction system from the work of Barb et al. was modelled [44]. The rate constants for the system were obtained from the work of Amme et al. [45]. The resulting chemical yields from the kinetic reaction system for Fe^{3+} are summarized in Table 3. The theoretical G-value of the Fricke dosimeter is reproduced to a high degree of accuracy, apart from under very high dose rates, where consumption of the initially present Fe^{2+} affects the results.

3.1.2. Diffusion

The diffusion calculation method was benchmarked through comparison with the analytical Ogata Banks solution to the transport equation [46]. This was done through the use of Dirichlet boundary condition on the inner boundary, meaning a fixed concentration at the boundary. This allows for comparison of the diffusion rate out into the bulk solution and the magnitude of this diffusion in relation to the boundary condition. The comparison between the implicit model used in this work and the analytical solution in a 10^4 μm system with 100 layers modelled for 10^4 time steps of 0.36 s each is shown in Fig. 2. The difference is very small, which shows that the implicit method used in this work can accurately describe the diffusion process.

3.2. Full solution reaction set

Using the full reaction set (Table S1, supplementary material), the concentration profiles across the water layers in a 1 mm system with 50 μm layer size under an α-dose rate of 1 Gy/h modelled for 10^4 time steps of 10 s each is shown in Fig. 3a. The initial time steps show significant concentration gradients across the layers of the system, Fig. 3b. Towards the end of the simulation time,
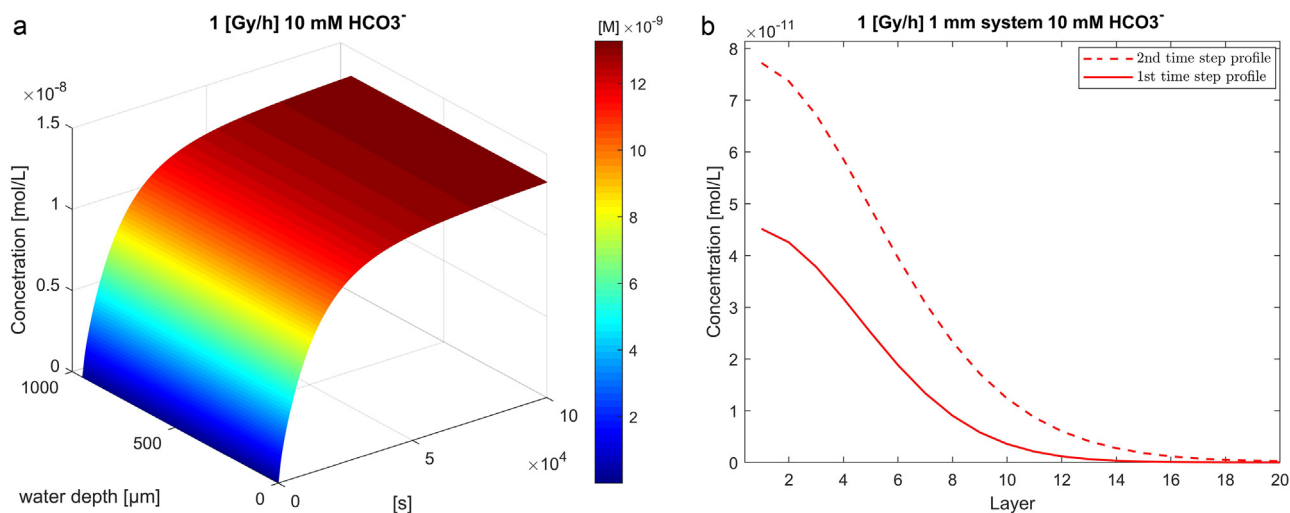
Fig. 3. (a) Concentration profile in a 1 mm water depth system with 50 μm layer size modelled for 10^4 steps of 10 s each. (b) Concentration profile across the water layers for the first and second time steps.

the system is in steady-state and shows a miniscule concentration gradient and H_2O_2 concentration increase per time step.

3.3. Comparison of full and simplified solution reaction set

Simulations taking both the temporal and spatial resolutions into account can become computationally demanding when employing the full set of chemical reactions. Since the concentration of H_2O_2 in a solution irradiated with alpha-radiation can usually be calculated by simply multiplying the absorbed dose and the G-value for H_2O_2, provided there are no reactions consuming H_2O_2, we have explored the validity of this simplification as a function of dose rate. The dose rate dependence was explored to make sure that errors are not introduced when using dose rate profiles in combination with the simplified description of the aqueous radiation chemistry. The simulations show that the difference, in terms of H_2O_2 concentration between the full reaction set and the simplified approach within the dose rate range of relevance here (1 - 10^3 Gy/h) is rather small, with the full reaction set giving somewhat lower concentrations (<20%). (The relative concentrations between the two reaction sets as a function of dose rate can be seen in Figure S2, supplementary material.)

To simulate the heterogeneous system, the rate constant for H_2O_2 consumption on UO_2 determined by Hossain et al. [18] was used. The rate constant is the sum of the rate constant for UO_2 oxidation and the rate constant for catalytic H_2O_2 decomposition. At the time this rate constant was determined, it was in general assumed that catalytic decomposition of H_2O_2 constituted 20% of the overall rate constant. The dissolved H_2O_2 and U(VI) concentrations were modelled with the full and the simplified reaction sets, in a 50 μm water depth system with 10 μm layer size modelled for 10 and 100 s time steps respectively for a total time of 10^5 s. The results are shown in Fig. 4. Using the full reaction set, the H_2O_2 steady-state concentration is asymptotically approached.

The simplified reaction set corresponds quite well with the full reaction set in terms of H_2O_2 concentration. The importance of using a fine temporal resolution is apparent, as a somewhat higher H_2O_2 concentration is obtained using the relatively rough time step of 100 s. This difference is due to a consumption of H_2O_2 in the innermost layer during the relatively long kinetic step prior to the diffusion step. The innermost layer can this way become depleted during the kinetic step as compared to the outer layers, leading to a lower overall consumption of H_2O_2 and higher steady-state concentration. The comparison shows that the simplified re-
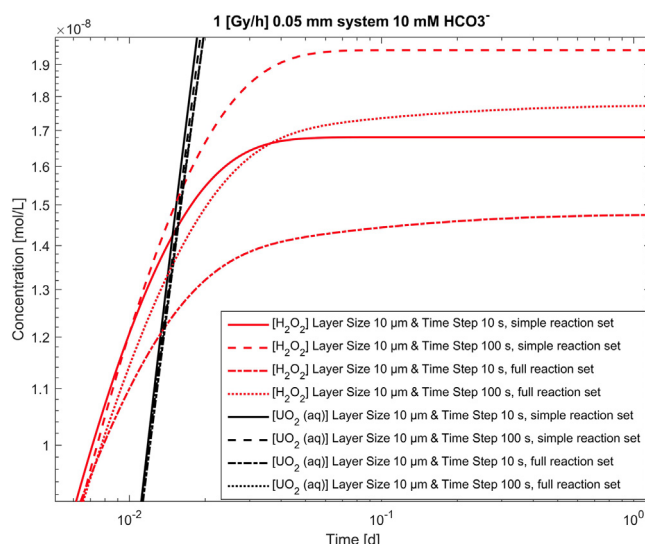

Fig. 4. Concentration evolution in the first layer of a 50 μm system with 10 μm layer size and 10 and 100 s time steps using the simplified and full reaction sets.

action set can describe the radiolytic oxidative dissolution of the full reaction set rather accurately. The reactions between the radiolytic species in solution therefore only causes a slight reduction in the H_2O_2 concentration. This could however change in groundwater with a more complicated composition

3.4. Simplified solution reaction system

The simplified reaction system consisting of only the radiolytic production of H_2O_2 and the rate constant $k_{U1}=4.6\cdot10^{-6}$ m·min^{-1} for the reaction between H_2O_2 and UO_2 from the work of Hossain et al. [18], accounting for 20% catalytic decomposition, were used to explore the impact of variations in model parameters, such as layer size and time step size. The simplified approach allows for a straightforward theoretical prediction of the H_2O_2 steady-state concentration as [17,47]:

$$[H_2O_2]_{ss} = \frac{r_{H_2O_2}}{k_{U1}} \cdot \delta_{max} \qquad (13)$$

For an α-dose rate of 1 Gy/h with α-particle energy of 5.5 MeV and range in H_2O δ_{max}=44 μm, Eq. (12) yields a theoretical

Table 4

Comparison of time to reach steady-state, resulting H_2O_2 and UO_2 concentrations as a function of time step and layer size with normal and averaged dose rate profiles in a 50 μm water depth system modelled for 10^4 s total.

|	Normal dose rate profile				Averaged dose rate profile			
Layer size [μm]			2.5					
$t_{stepsize}$ [s]	2	10	20	100	2	10	20	100
$t_{ss,99.9\%}$ [s]	4704	5270	6020	9800	4704	5270	6020	9800
$[H_2O_2]$	$1.69 \cdot 10^{-8}$	$1.86 \cdot 10^{-8}$	$2.09 \cdot 10^{-8}$	$4.53 \cdot 10^{-8}$	$1.70 \cdot 10^{-8}$	$1.90 \cdot 10^{-8}$	$2.17 \cdot 10^{-8}$	$5.02 \cdot 10^{-8}$
$[U(VI)(aq)]$	$1.86 \cdot 10^{-7}$	$1.85 \cdot 10^{-7}$	$1.82 \cdot 10^{-7}$	$1.63 \cdot 10^{-7}$	$1.86 \cdot 10^{-7}$	$1.84 \cdot 10^{-7}$	$1.82 \cdot 10^{-7}$	$1.59 \cdot 10^{-7}$
Layer size [μm]			5					
$t_{stepsize}$ [s]	2	10	20	100	2	10	20	100
$t_{ss,99.9\%}$ [s]	4634	4900	5240	8200	4634	4900	5240	8200
$[H_2O_2]$	$1.67 \cdot 10^{-8}$	$1.74 \cdot 10^{-8}$	$1.82 \cdot 10^{-8}$	$2.67 \cdot 10^{-8}$	$1.67 \cdot 10^{-8}$	$1.77 \cdot 10^{-8}$	$1.89 \cdot 10^{-8}$	$3.05 \cdot 10^{-8}$
$[U(VI)(aq)]$	$1.86 \cdot 10^{-7}$	$1.86 \cdot 10^{-7}$	$1.85 \cdot 10^{-7}$	$1.78 \cdot 10^{-7}$	$1.86 \cdot 10^{-7}$	$1.86 \cdot 10^{-7}$	$1.85 \cdot 10^{-7}$	$1.75 \cdot 10^{-7}$
Layer size [μm]			10					
$t_{stepsize}$ [s]	2	10	20	100	2	10	20	100
$t_{ss,99.9\%}$ [s]	4600	4720	4860	6200	4600	4720	4860	6200
$[H_2O_2]$	$1.66 \cdot 10^{-8}$	$1.68 \cdot 10^{-8}$	$1.71 \cdot 10^{-8}$	$1.95 \cdot 10^{-8}$	$1.66 \cdot 10^{-8}$	$1.70 \cdot 10^{-8}$	$1.76 \cdot 10^{-8}$	$2.22 \cdot 10^{-8}$
$[U(VI)(aq)]$	$1.86 \cdot 10^{-7}$	$1.86 \cdot 10^{-7}$	$1.86 \cdot 10^{-7}$	$1.84 \cdot 10^{-7}$	$1.86 \cdot 10^{-7}$	$1.86 \cdot 10^{-7}$	$1.86 \cdot 10^{-7}$	$1.82 \cdot 10^{-7}$
Layer size [μm]			25					
$t_{stepsize}$ [s]	2	10	20	100	2	10	20	100
$t_{ss,99.9\%}$ [s]	4580	4610	4660	5000	4580	4610	4660	5000
$[H_2O_2]$	$1.66 \cdot 10^{-8}$	$1.66 \cdot 10^{-8}$	$1.66 \cdot 10^{-8}$	$1.67 \cdot 10^{-8}$	$1.66 \cdot 10^{-8}$	$1.67 \cdot 10^{-8}$	$1.68 \cdot 10^{-8}$	$1.79 \cdot 10^{-8}$
$[U(VI)(aq)]$	$1.87 \cdot 10^{-7}$	$1.87 \cdot 10^{-7}$	$1.86 \cdot 10^{-7}$	$1.86 \cdot 10^{-7}$	$1.86 \cdot 10^{-7}$	$1.86 \cdot 10^{-7}$	$1.86 \cdot 10^{-7}$	$1.86 \cdot 10^{-7}$
Layer size [μm]			50					
$t_{stepsize}$ [s]	2	10	20	100	2	10	20	100
$t_{ss,99.9\%}$ [s]	4572	4580	4580	4600	4572	4580	4580	4600
$[H_2O_2]$	$1.66 \cdot 10^{-8}$	$1.66 \cdot 10^{-8}$	$1.66 \cdot 10^{-8}$	$1.66 \cdot 10^{-8}$	$1.66 \cdot 10^{-8}$	$1.66 \cdot 10^{-8}$	$1.66 \cdot 10^{-8}$	$1.66 \cdot 10^{-8}$
$[U(VI)(aq)]$	$1.87 \cdot 10^{-7}$	$1.87 \cdot 10^{-7}$	$1.86 \cdot 10^{-7}$	$1.87 \cdot 10^{-7}$	$1.87 \cdot 10^{-7}$	$1.87 \cdot 10^{-7}$	$1.86 \cdot 10^{-7}$	$1.87 \cdot 10^{-7}$
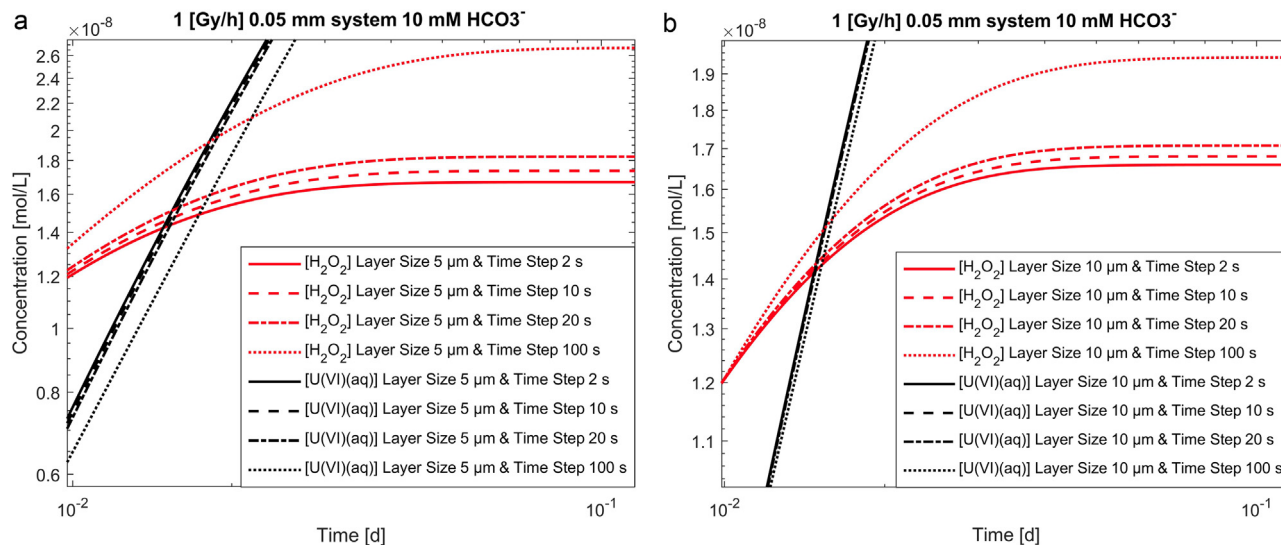
Fig. 5. Influence of time step-size on the H_2O_2 steady-state concentration in the first layer of 50 μm water depth system with 5 μm (a) and 10 μm layer size (b).

steady-state concentration of $\sim 1.66 \cdot 10^{-8}$ M. Closed systems with 50 μm and 1 mm total water layer thickness were modelled for total times of 10^4 and 10^5 s, respectively, using varying time steps and layer sizes. System averaged H_2O_2 steady-state concentrations, the time to reach 99.9% of the steady-state value, and final system averaged dissolved uranium concentrations are presented in Tables 4 and 5 for the 50 μm and 1 mm systems respectively. Concentration profiles for a few time resolutions and layer sizes in the 50 μm and 1 mm systems are shown in Figs. 5 and 6 respectively.

The effect of dose rate profile resolution was also studied. The comparison was made between a high resolution dose rate profile and an averaged dose rate over the innermost 50 μm water

layers. The results are shown in Tables 4 and 5. The systems can be homogenized without any loss of accuracy of the H_2O_2 steady-state concentration. A very small influence of averaged dose rate profile can be observed in the steady-state concentrations. The difference is more pronounced in the systems with higher spatial resolution, i.e., smaller layer size, as the dose rate profile resolution is constrained by the layer size. The effect is somewhat more pronounced in the 50 μm system as compared to the 1 mm system. The deviation from the theoretical steady-state concentration of $1.66 \cdot 10^{-8}$ can be seen as layer size assumes small values combined with large time step sizes. This deviation becomes evident when the time step size assumes values of approximately equal to

Table 5

Comparison of time to reach steady-state, resulting H_2O_2 and UO_2 concentrations as a function of time step and layer size with normal and averaged dose rate profiles in a 1 mm water depth system modelled for 10^5 s total.

|	Normal dose rate profile				Averaged dose rate profile			
Layer size [µm]			5					
$t_{stepsize}$ [s]	2	20	100	200	2	20	100	200
$t_{ss,99.9\%}$ [s]	87,088	92,220	98,800	99,600	87,090	92,220	98,800	99,600
$[H_2O_2]$	$1.68 \cdot 10^{-8}$	$1.82 \cdot 10^{-8}$	$2.62 \cdot 10^{-8}$	$3.64 \cdot 10^{-8}$	$1.67 \cdot 10^{-8}$	$1.89 \cdot 10^{-8}$	$2.99 \cdot 10^{-8}$	$4.44 \cdot 10^{-8}$
$[U(VI)(aq)]$	$8.66 \cdot 10^{-8}$	$8.56 \cdot 10^{-8}$	$7.89 \cdot 10^{-8}$	$7.07 \cdot 10^{-8}$	$8.65 \cdot 10^{-8}$	$8.48 \cdot 10^{-8}$	$7.60 \cdot 10^{-8}$	$6.44 \cdot 10^{-8}$
Layer size [µm]			10					
$t_{stepsize}$ [s]	2	20	100	200	2	20	100	200
$t_{ss,99.9\%}$ [s]	86,732	89,580	96,600	98,800	86,732	89,580	96,600	98,800
$[H_2O_2]$	$1.66 \cdot 10^{-8}$	$1.71 \cdot 10^{-8}$	$1.94 \cdot 10^{-8}$	$2.26 \cdot 10^{-8}$	$1.66 \cdot 10^{-8}$	$1.76 \cdot 10^{-8}$	$2.21 \cdot 10^{-8}$	$2.84 \cdot 10^{-8}$
$[U(VI)(aq)]$	$8.66 \cdot 10^{-8}$	$8.66 \cdot 10^{-8}$	$8.45 \cdot 10^{-8}$	$8.16 \cdot 10^{-8}$	$8.64 \cdot 10^{-8}$	$8.56 \cdot 10^{-8}$	$8.23 \cdot 10^{-8}$	$7.73 \cdot 10^{-8}$
Layer size [µm]			25					
$t_{stepsize}$ [s]	2	20	100	200	2	20	100	200
$t_{ss,99.9\%}$ [s]	86,506	87,640	92,100	95,600	86,506	87,640	92,100	95,600
$[H_2O_2]$	$1.65 \cdot 10^{-8}$	$1.66 \cdot 10^{-8}$	$1.67 \cdot 10^{-8}$	$1.68 \cdot 10^{-8}$	$1.65 \cdot 10^{-8}$	$1.68 \cdot 10^{-8}$	$1.78 \cdot 10^{-8}$	$1.92 \cdot 10^{-8}$
$[U(VI)(aq)]$	$8.68 \cdot 10^{-8}$	$8.68 \cdot 10^{-8}$	$8.67 \cdot 10^{-8}$	$8.66 \cdot 10^{-8}$	$8.66 \cdot 10^{-8}$	$8.66 \cdot 10^{-8}$	$8.58 \cdot 10^{-8}$	$8.46 \cdot 10^{-8}$
Layer size [µm]			100					
$t_{stepsize}$ [s]	2	20	100	200	2	20	100	200
$t_{ss,99.9\%}$ [s]	86,366	86,540	87,700	89,200	86,366	86,540	87,700	89,200
$[H_2O_2]$	$1.65 \cdot 10^{-8}$	$1.65 \cdot 10^{-8}$	$1.65 \cdot 10^{-8}$	$1.65 \cdot 10^{-8}$	$1.65 \cdot 10^{-8}$	$1.65 \cdot 10^{-8}$	$1.65 \cdot 10^{-8}$	$1.65 \cdot 10^{-8}$
$[U(VI)(aq)]$	$8.68 \cdot 10^{-8}$	$8.68 \cdot 10^{-8}$	$8.68 \cdot 10^{-8}$	$8.68 \cdot 10^{-8}$	$8.68 \cdot 10^{-8}$	$8.68 \cdot 10^{-8}$	$8.68 \cdot 10^{-8}$	$8.68 \cdot 10^{-8}$
Layer size [µm]			1000					
$t_{stepsize}$ [s]	2	20	100	200	2	20	100	200
$t_{ss,99.9\%}$ [s]	85,862	85,880	85,900	86,000	85,862	85,880	85,900	86,000
$[H_2O_2]$	$1.65 \cdot 10^{-8}$	$1.65 \cdot 10^{-8}$	$1.65 \cdot 10^{-8}$	$1.65 \cdot 10^{-8}$	$1.65 \cdot 10^{-8}$	$1.65 \cdot 10^{-8}$	$1.65 \cdot 10^{-8}$	$1.65 \cdot 10^{-8}$
$[U(VI)(aq)]$	$8.68 \cdot 10^{-8}$	$8.68 \cdot 10^{-8}$	$8.68 \cdot 10^{-8}$	$8.68 \cdot 10^{-8}$	$8.68 \cdot 10^{-8}$	$8.68 \cdot 10^{-8}$	$8.68 \cdot 10^{-8}$	$8.68 \cdot 10^{-8}$
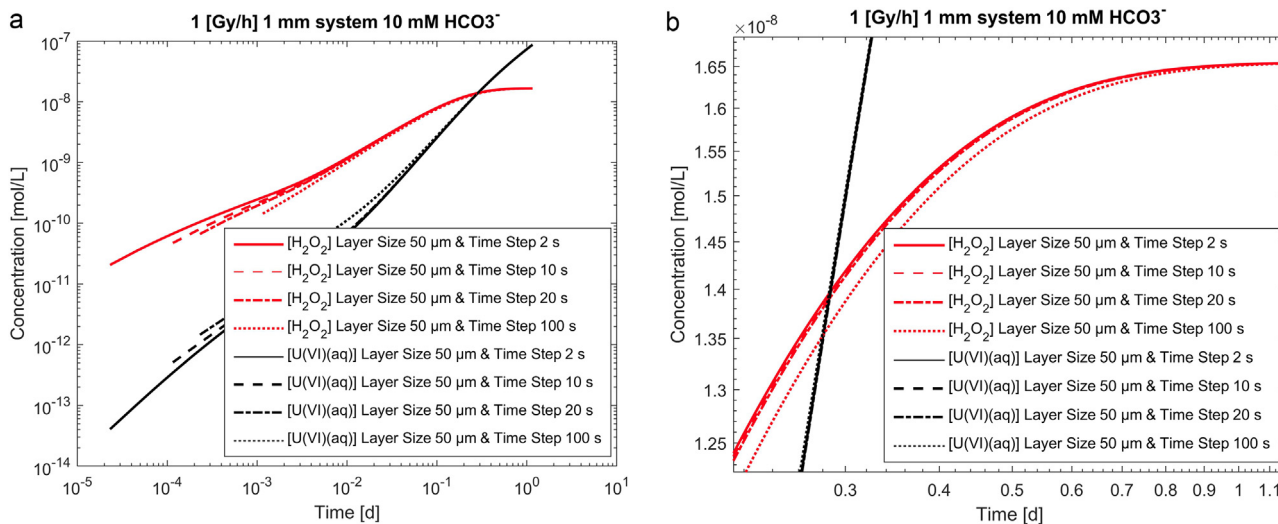
Fig. 6. Influence of time step-size on the H_2O_2 steady-state concentration in the first layer of a 1 mm depth 50 µm layer size system.

or larger than the layer size (in units s and µm respectively). This limitation is due to the fact that consumption of the radiolytically produced H_2O_2 occurs quickly in the small innermost layer. Depletion of H_2O_2 in the innermost layer during the time step results in an inaccurate and overall lower consumption, leading to a higher steady-state H_2O_2 value combined with a lower U(VI)(aq) concentration.

3.5. Radical species

Radical species are relatively short lived as compared to molecular species such as H_2O_2. The impact of the spatial and temporal resolutions might be significantly different with respect to the short lived species. Studying the concentration of OH· in the 50 µm system with a time step size of 10 s for 10^3 steps with varying spatial resolutions using the full reaction system is shown in Table 6. It is evident that the average OH-radical concentration is rather un-

Table 6

System averaged OH· concentration over the 50 µm system with 10^3 time steps of 10 s each and varying layer size.

$t_{stepsize}$ [s]			10	
Time steps	10^3	10^3	10^3	10^3
Layer size [µm]	5	10	25	50
[OH·]	$1.22 \cdot 10^{-16}$	$1.23 \cdot 10^{-16}$	$1.24 \cdot 10^{-16}$	$1.24 \cdot 10^{-16}$

Table 7
Fitted rate constants to the OH·(ads) surface reaction system.

$[H_2O_2]_0$	ks1 (M^{-1}·s^{-1})	ks2 (s^{-1})	ks3 (M^{-1}·s^{-1})	ks5 (M^{-1}·s^{-1})
0.2 mM	8.66·10^{-1}	5.48·10^{-1}	1.06·10^{2}	1.41·10^{1}
0.5 mM	5.03·10^{-1}	2.25·10^{-1}	1.76·10^{2}	2.23·10^{1}
1.0 mM	3.50·10^{-1}	2.09·10^{-1}	1.86·10^{2}	2.21·10^{1}
2.0 mM	2.33·10^{-1}	2.49·10^{-1}	1.96·10^{2}	2.42·10^{1}
Full system	4.62·10^{-1}	1.91·10^{-1}	1.97·10^{2}	3.41·10^{1}

affected by the change in layer size in the very small system. It should be emphasized that the effect of temporal and spatial resolution is rather weak in the small closed systems that are studied in this work. This is due to the fact that small systems using the no flux boundary conditions approaches a system with a relatively small gradient rather quickly.

3.6. Surface reaction systems

3.6.1. System fit

The experimental data from the work of Barreiro Fidalgo et al. [20] were used to fit the surface site reaction system, described in Table 2. An initial UO$_2$ surface site density of 2.1·10^{-4} mol/m^2 was used in the model [18]. The sum of the squares of the residual values was output by the lsqnonlin function using the reaction system function file with the rate constants as input. In the simultaneous fit of all data sets, weight factors normalizing the residuals from the individual data sets, according to the factor 2 mM/[H$_2$O$_2$]$_0$, were used. This means that the residuals of the data points in the [H$_2$O$_2$]$_0$ = 0.2 mM data set were multiplied by a factor 10 to make the weight of the data set the same as the [H$_2$O$_2$]$_0$ = 2.0 mM data set. Individual data set fits and the total system fit of all data sets were performed with stoichiometric UO$_2$ at t = 0. The rate constants were calculated with the specific surface to volume ratio, S/V=5400 m^{-1} system in the work of Barreiro Fidalgo *et al.* [20]. The fitted rate constants are shown in Table 7. The rate constants derived from the different initial concentrations vary somewhat, although the relative values of the constants are in quite good agreement. The results are somewhat insensitive to variations of the value of ks5, which can vary an order of magnitude while having a small impact on the dissolution rates and residual values. When applying the constants to a system, the S/V ratio of the specific system has to be taken into account as can be seen from the units of the constants [20].

The higher concentration data series are less reliable to fit the reaction mechanism as complexes between the dissolved uranium and H$_2$O$_2$ can significantly influence the kinetics of the aforementioned reactions [48]. Therefore, it is most important that the reaction set can accurately describe the low concentration series. The individual data series fit of [H$_2$O$_2$]$_0$ = 0.2 is shown in Fig. 7 (all the individual data series fits can be seen in Figure S1, supplementary material.) The weighted total system fit is shown in Fig. 8.

3.6.2. Impact of surface reaction mechanism

To explore the influence of the surface site reaction system (Full system, Table 7) as compared to using the oxidative dissolution rate constant of Hossain et al. [18], (80% oxidative dissolution and 20% catalytic decomposition), using the full reaction system in both cases, fuel models with dose rates of 1 Gy/h and 1 kGy/h respectively were studied in 50 μm system with 10 μm layer size for 10^4 time steps of 10 s each. The results are shown in Fig. 9. The reason for the slow dissolution in the surface site reaction system is due to the fact that U(V) needs to build up on the surface before U(VI) can form and dissolve into solution. The reason for the slow dissolution in the surface site reaction system is due to the fact that U(V) needs to build up on the
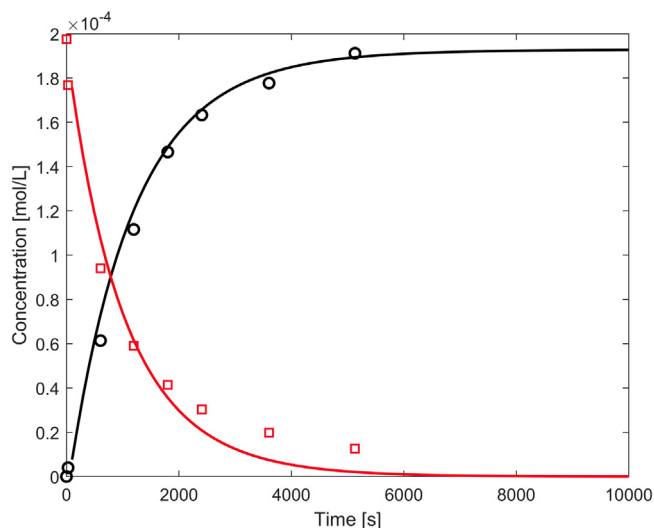

Fig. 7. Fit of the individual data series $[H_2O_2]_0$ = 0.2 of the Barreiro Fidalgo data with stoichiometric UO$_2$ at t = 0 with the constants k80, k81, k82 and k83 shown in Table 7.

surface before U(VI) can form and dissolve into solution. However, after an initial period, the dissolution rate is governed by the H$_2$O$_2$ production rate in both descriptions of the surface oxidation mechanism. The resulting H$_2$O$_2$ concentrations are 1.30·10^{-8} M and 1.47·10^{-8} M respectively for the 1 Gy/h fuel model using the surface site reaction system and the full reaction system (Table S1, supplementary material) with the Hossain et al. rate constant. This can be compared to the somewhat higher theoretical value of 1.66·10^{-8} M using the simplified system. At 1 Gy/h, the initial dissolution of uranium is significantly slower when using the surface site reaction system (7.54·10^{-11} mol/L·d) as compared to the full reaction system (5.96·10^{-8} mol/L·d). However, for longer times the dissolution rates become quite similar, 2.13·10^{-6} mol/L·d compared to 1.52·10^{-6} mol/L·d, respectively. At 1 kGy/h, the effect is less pronounced in relative terms, with initial dissolution rates of 4.16·10^{-5} mol/L·d and 5.68·10^{-5} mol/L·d and final dissolution rates of 2.14·10^{-3} mol/L·d and 2.07·10^{-3} mol/L·d, respectively. The reason for the difference in relative dissolution rates between the high and the low dose rate can be attributed to the fact that the fraction of H$_2$O$_2$ that undergoes catalytic decomposition depends on the H$_2$O$_2$ concentration and thereby on the dose rate in the surface site model while the fraction is always 20% in the traditional model. Using the 1 kGy/h fuel model the resulting H$_2$O$_2$ concentrations are 1.32·10^{-5} M and 2.02·10^{-5} M respectively for the surface site and Hossain et al. [18] rate constant reaction systems.

Results of the comparison between the normal dose rate profile and an averaged dose rate over the innermost 50 μm water layer using the surface site reaction system are shown in Table 8. A small influence of the averaged dose rate profile can be observed in the steady-state concentrations. The difference is more pronounced in the systems with higher spatial resolution, i.e., smaller layer size (as previously discussed for the simplified system, Tables 4 and 5). It is evident from both the simplified reaction system and surface site reaction system that large layer sizes and an averaged dose rate profile yields results in quite good agreement with the higher resolution systems. However, the amount of dissolved uranium is somewhat lower in the homogenized system (i.e., with a layer size of 50 μm) using the surface site reaction system as shown in Table 8. The deviation in the homogenized system stems from the fact that the H$_2$O$_2$ formed at the water layers close to the surface can rather quickly react with the surface. As the system is homogenized, a
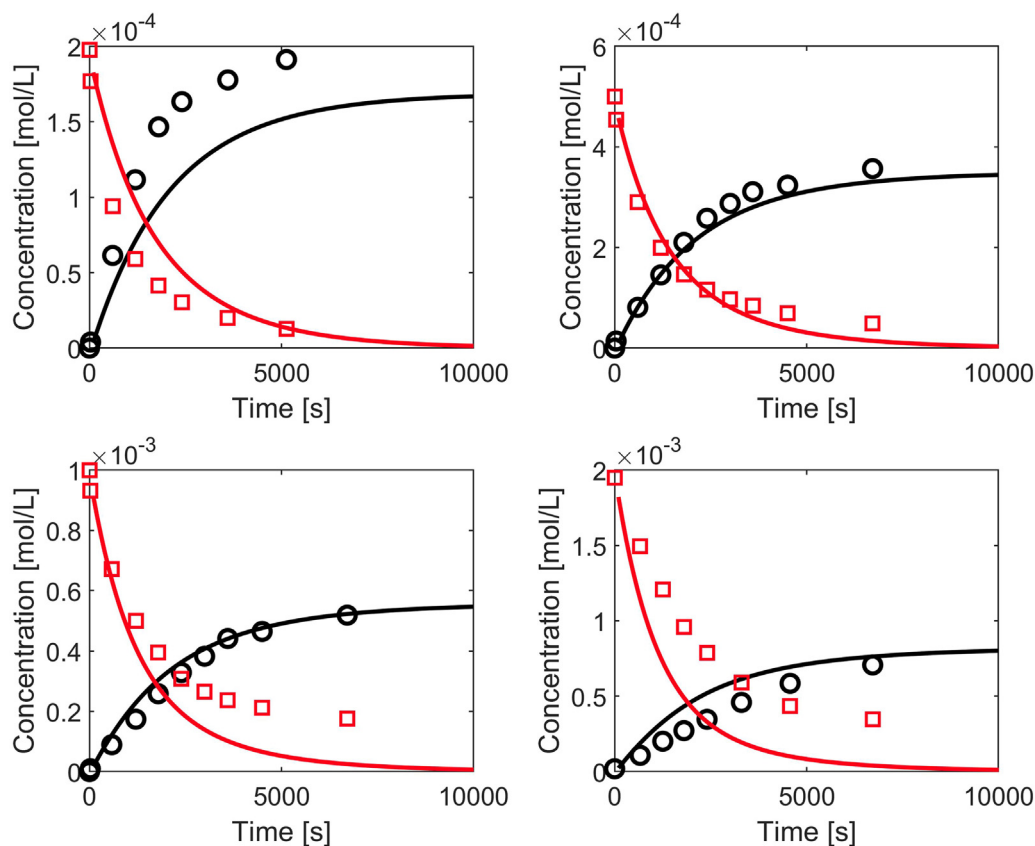
Fig. 8. Fits the total system of the Barreiro Fidalgo data with stoichiometric UO_2 at $t = 0$ with the constants k80, k81, k82 and k83 shown in Table 7.
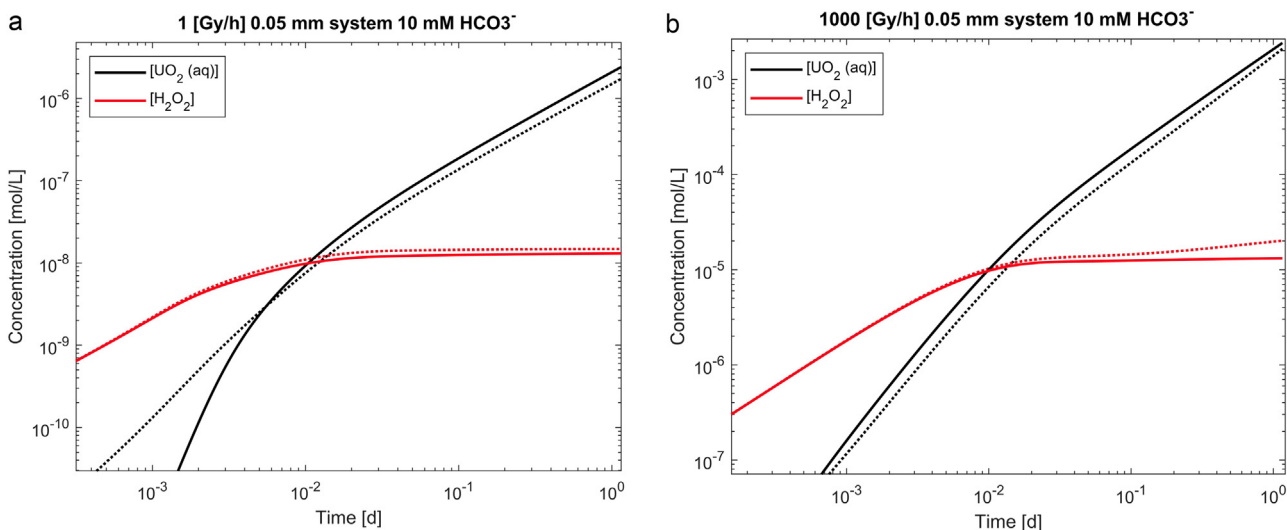

Fig. 9. 1 Gy/h (a) & 1 kGy/h (b) fuel models with the surface site reaction system (filled lines) and the rate constant from the work of Hossain et al. [18] (dotted lines) in the first layer in a 50 μm system with 10 μm layer size modelled for 10^4 steps of 10 s each with 10 mM HCO_3^-.

lower H_2O_2 concentration at the closest water layers are obtained which has a noticeable effect on the dissolution.

3.7. Comparison with literature data

The model was also used to simulate the experiment of Sattonnay *et al.*, in which UO_2 in contact with deionized aerated water was irradiated by a high energy cyclotron α-particle beam, resulting in fluxes of $3.3 \cdot 10^{10}$ and $3.3 \cdot 10^{11}$ $\alpha \cdot cm^{-2} \cdot s^1$ with 5 MeV α-particle energy [7]. The resulting dose rate in the inner 40 μm

layer was therefore $2.37 \cdot 10^8$ Gy/h [49]. The irradiated volume in the experiment was 10 mL with a surface area of 0.2827 cm^2, which for the 1 h duration gives a total specific H_2O_2 production of $2.79 \cdot 10^{-4}$ and $2.79 \cdot 10^{-3}$ M using the primary yield (in Table 1) for the weaker and stronger fluxes respectively. As the concentration measurements were averaged for the entire solutions in the work of the authors, the system was simulated as a homogeneous system using the rate constant for H_2O_2 consumption on UO_2 determined by Hossain et al. [18] (80% oxidative dissolution and 20% catalytic decomposition) and the surface site reaction system.

Table 8

50 μm water depth system with a 1 Gy/h α-dose rate source using the total system fit of the surface site reaction system.

	Normal dose rate profile				Averaged dose rate profile			
Layer size [μm]				5				
$t_{stepsize}$ [s]	2	10	20	100	2	10	20	100
$t_{ss,99.9\%}$ [s]	9618	9630	9640	9800	9618	9630	9620	9700
$[H_2O_2]$	$1.24 \cdot 10^{-8}$	$1.30 \cdot 10^{-8}$	$1.38 \cdot 10^{-8}$	$2.16 \cdot 10^{-8}$	$1.25 \cdot 10^{-8}$	$1.33 \cdot 10^{-8}$	$1.45 \cdot 10^{-8}$	$2.53 \cdot 10^{-8}$
$[U(VI)(aq)]$	$2.20 \cdot 10^{-7}$	$2.19 \cdot 10^{-7}$	$2.19 \cdot 10^{-7}$	$2.11 \cdot 10^{-7}$	$2.20 \cdot 10^{-7}$	$2.19 \cdot 10^{-7}$	$2.18 \cdot 10^{-7}$	$2.07 \cdot 10^{-7}$
Layer size [μm]				10				
$t_{stepsize}$ [s]	2	10	20	100	2	10	20	100
$t_{ss,99.9\%}$ [s]	9616	9620	9620	9700	9616	9620	9600	9600
$[H_2O_2]$	$1.23 \cdot 10^{-8}$	$1.25 \cdot 10^{-8}$	$1.28 \cdot 10^{-8}$	$1.50 \cdot 10^{-8}$	$1.24 \cdot 10^{-8}$	$1.28 \cdot 10^{-8}$	$1.33 \cdot 10^{-8}$	$1.76 \cdot 10^{-8}$
$[U(VI)(aq)]$	$2.19 \cdot 10^{-7}$	$2.19 \cdot 10^{-7}$	$2.19 \cdot 10^{-7}$	$2.18 \cdot 10^{-7}$	$2.19 \cdot 10^{-7}$	$2.19 \cdot 10^{-7}$	$2.19 \cdot 10^{-7}$	$2.15 \cdot 10^{-7}$
Layer size [μm]				25				
$t_{stepsize}$ [s]	2	10	20	100	2	10	20	100
$t_{ss,99.9\%}$ [s]	9614	9620	9620	9600	9614	9610	9600	9600
$[H_2O_2]$	$1.23 \cdot 10^{-8}$	$1.23 \cdot 10^{-8}$	$1.23 \cdot 10^{-8}$	$1.25 \cdot 10^{-8}$	$1.23 \cdot 10^{-8}$	$1.24 \cdot 10^{-8}$	$1.26 \cdot 10^{-8}$	$1.36 \cdot 10^{-8}$
$[U(VI)(aq)]$	$2.14 \cdot 10^{-7}$	$2.14 \cdot 10^{-7}$	$2.14 \cdot 10^{-7}$	$2.15 \cdot 10^{-7}$	$2.14 \cdot 10^{-7}$	$2.14 \cdot 10^{-7}$	$2.14 \cdot 10^{-7}$	$2.14 \cdot 10^{-7}$
Layer size [μm]				50				
$t_{stepsize}$ [s]	2	10	20	100	2	10	20	100
$t_{ss,99.9\%}$ [s]	9610	9610	9620	9700	9610	9610	9620	9700
$[H_2O_2]$	$1.22 \cdot 10^{-8}$	$1.22 \cdot 10^{-8}$	$1.22 \cdot 10^{-8}$	$1.22 \cdot 10^{-8}$	$1.22 \cdot 10^{-8}$	$1.22 \cdot 10^{-8}$	$1.22 \cdot 10^{-8}$	$1.22 \cdot 10^{-8}$
$[U(VI)(aq)]$	$2.00 \cdot 10^{-7}$	$2.00 \cdot 10^{-7}$	$2.00 \cdot 10^{-7}$	$2.00 \cdot 10^{-7}$	$2.00 \cdot 10^{-7}$	$2.00 \cdot 10^{-7}$	$2.00 \cdot 10^{-7}$	$2.00 \cdot 10^{-7}$

The resulting H_2O_2 concentration is $2.28 \cdot 10^{-3}$ M using both the Hossain et al. constant and the surface site reaction system. This is rather close to the concentration calculated from the primary yields, as well as the concentration found in the measurement of the authors, of $(3.5 \pm 0.3) \cdot 10^{-3}$ M. The modelled uranium concentration using the Hossain et al., constant is more than an order of magnitude lower than the measured value, $7.18 \cdot 10^{-7}$ M compared to $9.58 \cdot 10^{-6}$ M. The value of the dissolved uranium using the surface site reaction system is significantly lower, of $2.5 \cdot 10^{-8}$ M. This is as previously discussed due to the dependence of U(V) build up on the surface which is slower in the system of Sattonnay et al., due to the smaller S/V ratio. This might be due to the fact that ks5 is not rate determining in the fitted reaction system, meaning that the value could potentially be significantly larger than the fitted value. Therefore, increasing the value of ks5 is a reasonable approach to remove the rate determining effect of this reaction that is present in systems with a smaller S/V ratio. In order to test the effect of increasing the value of ks5 in the system, a value of 10^{10} $M^{-1} \cdot s^{-1}$ was tested. This yields the same H_2O_2 concentration of $2.28 \cdot 10^{-3}$ M and a uranium concentration of $3.13 \cdot 10^{-7}$ M. The influence of ks5 can therefore not explain the difference between the modelled values and the experimental ones. This indicates an underestimation by the model, or an increased release rate in the cyclotron experiment potentially due to the significantly lower pH-value [7]. The results of the modelling of the stronger flux are shown in Fig. 10.

The cyclotron experiment by Sattonnay et al. was modelled in the work of Christensen, where an underestimation in the uranium dissolution by a factor 40 was found [50]. The experiment was also modelled in the work of Poulesquen and Jégou, where the system was modelled as a system of 2 mm depth with 200 layers with time steps of 0.05 s for a total time of 3600 s [49]. The results show some discrepancy between the uranium concentrations in the layers closest to the surface and the experimental results of Sattonnay et al. [7,49]. However, the modelled system in the work of Poulesquen and Jégou show a very strong concentration gradient, where the outer layers have uranium concentrations in line with the experimental values. The concentrations in the outer layer were chosen in the work by the authors for comparison instead of the averaged value [49], while the latter would be a more relevant comparison to the experimental method of Sattonnay et al.
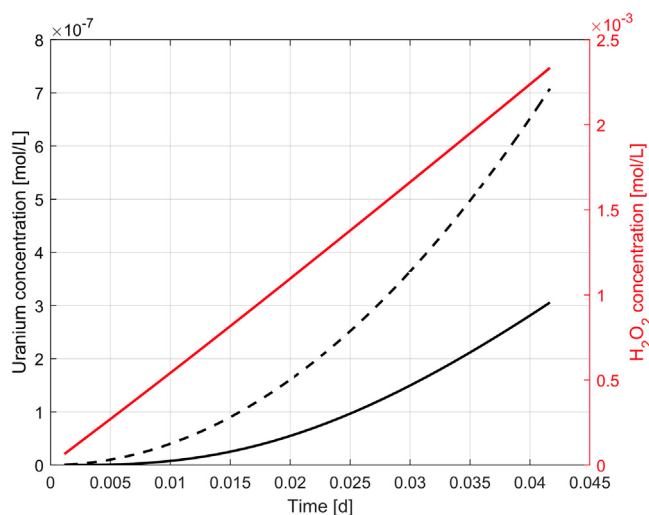

Fig. 10. Dissolved uranium and H_2O_2 production rates under the $2.37 \cdot 10^8$ Gy/h dose rate simulating the cyclotron experiment with flux $3.3 \cdot 10^{11}$ $\alpha \cdot cm^{-2} \cdot s^{-1}$ in the work of Sattonnay et al. [7]. The Hossain et al., rate constant is shown in the dashed lines and the surface site reaction system is shown as solid lines.

[7]. The strong gradient in the work of Poulesquen and Jégou is not seen when modelling the same system with the model developed in this work, as the diffusion is sufficiently fast (see Fig. 2) to create an almost homogenized system in the rather small closed system using the no flux boundary conditions.

Modelling was also performed of the experiments from the work of Cobos et al. [51], where α-doped UO_2 pellets with α-activities of $3.8 \cdot 10^7$, $3.8 \cdot 10^8$, and $3.8 \cdot 10^{10}$ Bq/g were studied in 35 mL deionized water solution. The system was also homogenized in the modelling to describe the rather small system in which diffusion will play a negligible role over the rather long modelled time scales. The dissolved uranium amounts after ~ 1700 h in the work of Cobos et al. under exposure to the $3.8 \cdot 10^7$, $3.8 \cdot 10^8$, and $3.8 \cdot 10^{10}$ Bq/g sources were modelled. The comparison between the results using the model in this work and the experimental dissolved uranium data can be seen in Table 9. The models can rather accurately predict the release of the $3.8 \cdot 10^{10}$ Bq/g source but is

Table 9

Comparison between the experimental and modelled dissolved uranium amounts of the α-doped UO_2 of Cobos et al. [51], using the model developed in this work. Both the rate constant from the work of Hossain et al., and the surface site reaction system were used.

A [Bq/g]	Cobos et al. [51] [mol]	Hossain et al., constant [mol]	Surface site model [mol]
$3.8 \cdot 10^{10}$	$1.3 \cdot 10^{-6}$	$2.68 \cdot 10^{-6}$	$3.6 \cdot 10^{-6}$
$3.8 \cdot 10^{8}$	$2.0 \cdot 10^{-7}$	$3.00 \cdot 10^{-8}$	$4.6 \cdot 10^{-8}$
$3.8 \cdot 10^{7}$	$3.0 \cdot 10^{-8}$	$2.85 \cdot 10^{-9}$	$4.0 \cdot 10^{-9}$

worse at predicting the releases from the weaker sources. In the experimental work, the uranium release is not only attributed to water radiolysis. Background dissolution due to the pre-existence of uranium in oxidation state higher than U(IV) or due to traces of oxygen in the solution will have a larger relative impact at lower specific activities. While the specific activities differ by three orders of magnitude, the experimental rate of dissolution only differs by a factor of 40, i.e., less than two orders of magnitude. In the simulations, only radiation-induced oxidative dissolution is included, and does not take these other effects into account.

4. Conclusions

From the tests of the performance of the numerical model it is clear that both spatial and temporal resolution influence the simulations. What is particularly important is the fact that the temporal resolution must be adapted to the spatial resolution in order to avoid divergence from the theoretically predicted steady-state values of H_2O_2. Additionally, very rough spatial resolution in the surface site reaction system led to an underestimation of the UO_2 dissolution due to a lower H_2O_2 concentration at the layers closest to the surface.

The simulations performed using the full reaction set and a simplified system accounting only for H_2O_2 production in the aqueous phase are in reasonably good agreement regarding the evolution of H_2O_2 and U(VI)(aq) concentrations. Consequently, the simplified system can be used in order to test model parameters such as the time to reach steady-state, with much less computational demand.

The surface site reaction system accounts for the experimental observations of surface-bound hydroxyl radical as well as the formation of U(V) in the oxidative dissolution reaction. The surface site reaction system could further be used to test the effects of species reacting with the surface bound OH-radicals.

Data availability

Data included in the present study are available from the corresponding author upon request.

Declaration of competing interest

Niklas L. Hansson reports financial support was provided by Swedish Nuclear Fuel and Waste Management Co. Niklas L. Hansson reports a relationship with Swedish Nuclear Fuel and Waste Management Co that includes: funding grants.

CRediT authorship contribution statement

N.L. Hansson: Conceptualization, Formal analysis, Investigation, Methodology, Software, Validation, Visualization, Writing – original draft. **M. Jonsson:** Conceptualization, Methodology, Project administration, Supervision, Validation, Writing – review & editing. **C. Ekberg:** Conceptualization, Funding acquisition, Resources, Supervision, Writing – review & editing. **K. Spahiu:** Conceptualization, Funding acquisition, Supervision, Writing – review & editing.

Data Availability

Data will be made available on request.

Supplementary materials

Supplementary material associated with this article can be found, in the online version, at doi:10.1016/j.jnucmat.2023.154369.

References

[1] E. Ekeroth, O. Roth, M. Jonsson, The relative impact of radiolysis products in radiation induced oxidative dissolution of UO2, J. Nucl. Mater. 355 (2006) 38–46, doi:10.1016/j.jnucmat.2006.04.001.

[2] C.M. Lousada, M. Trummer, M. Jonsson, Reactivity of H2O2 towards different UO2-based materials: the relative impact of radiolysis products revisited, J. Nucl. Mater. 434 (2013) 434–439, doi:10.1016/j.jnucmat.2011.06.003.

[3] R. Guillaumont, T. Fanghanel, I. Grenthe, V. Neck, D. Palmer, M. Rand, Update on the chemical thermodynamics of uranium, neptunium, plutonium, americium and technetium, Nuclear Energy Agency Data Bank, Organization for Economic Co-operation, Development 5 (2003).

[4] S. Sunder, Calculation of radiation dose rates in a water layer in contact with used CANDU UO_2 fuel, Nucl. Technol. 122 (1998) 211–221, doi:10.13182/NT98-A2863.

[5] L. Bauhn, N. Hansson, C. Ekberg, P. Fors, R. Delville, K. Spahiu, The interaction of molecular hydrogen with α-radiolytic oxidants on a (U,Pu)O₂ surface, J. Nucl. Mater. 505 (2018) 54–61, doi:10.1016/j.jnucmat.2018.04.006.

[6] C. Jegou, B. Muzeau, V. Broudic, S. Peuget, A. Poulesquen, D. Roudil, C. Corbel, Effect of external gamma irradiation on dissolution of the spent UO2 fuel matrix, J. Nucl. Mater. 341 (2005) 62–82, doi:10.1016/j.jnucmat.2005.01.008.

[7] G. Sattonnay, C. Ardois, C. Corbel, J. Lucchini, M.-F. Barthe, F. Garrido, D. Gosset, Alpha-radiolysis effects on UO_2 alteration in water, J. Nucl. Mater. 288 (2001) 11–19, doi:10.1016/S0022-3115(00)00714-5.

[8] V. Kerleguer, C. Jégou, L. De Windt, V. Broudic, G. Jouan, S. Miro, F. Tocino, C. Martin, The mechanisms of alteration of a homogeneous U0. 73Pu0. 27O2 MOx fuel under alpha radiolysis of water, J. Nucl. Mater. 529 (2020) 151920, doi:10.1016/j.jnucmat.2019.151920.

[9] A. Siberry, D. Hambley, A. Adamska, R. Springell, A mathematical model to describe the alpha dose rate from a UO_2 surface, Radiat. Phys. Chem. 182 (2021) 109359, doi:10.1016/j.radphyschem.2021.109359.

[10] N. Hansson, C. Ekberg, K. Spahiu, Alpha dose rate calculations for UO_2 based materials using stopping power models, Nucl. Mater. Energy 22 (2020) 100734, doi:10.1016/j.nme.2020.100734.

[11] N. Hansson, M. Jonsson, C. Ekberg, K. Spahiu, Geometrical aspects of alpha dose rates from UO2 based fuels, Radiat. Phys. Chem. 199 (2022) 110336, doi:10.1016/j.radphyschem.2022.110336.

[12] M. Trummer, M. Jonsson, Resolving the H2 effect on radiation induced dissolution of UO2-based spent nuclear fuel, J. Nucl. Mater. 396 (2010) 163–169, doi:10.1016/j.jnucmat.2009.10.067.

[13] B. Pastina, J.A. LaVerne, Effect of molecular hydrogen on hydrogen peroxide in water radiolysis, J. Phys. Chem. A 105 (2001) 9316–9322, doi:10.1021/jp012245j.

[14] L. Wu, N. Liu, Z. Qin, D.W. Shoesmith, Modeling the radiolytic corrosion of fractured nuclear fuel under permanent disposal conditions, J. Electrochem. Soc. 161 (2014) E3259, doi:10.1149/2.032408jes.

[15] O. Roth, M. Jonsson, Oxidation of UO2 (s) in aqueous solution, Cent. Eur. J. Chem. 6 (2008) 1–14, doi:10.2478/s11532-007-0067-z.

[16] E. Ekeroth, M. Jonsson, Oxidation of UO2 by radiolytic oxidants, J. Nucl. Mater. 322 (2003) 242–248, doi:10.1016/j.jnucmat.2003.07.001.

[17] M. Jonsson, F. Nielsen, O. Roth, E. Ekeroth, S. Nilsson, M.M. Hossain, Radiation induced spent nuclear fuel dissolution under deep repository conditions, Environ. Sci. Technol. 41 (2007) 7087–7093, doi:10.1021/es070832y.

[18] M.M. Hossain, E. Ekeroth, M. Jonsson, Effects of HCO3-on the kinetics of UO2 oxidation by H2O2, J. Nucl. Mater. 358 (2006) 202–208, doi:10.1016/j.jnucmat. 2006.07.008.

[19] M. Jonsson, E. Ekeroth, O. Roth, Dissolution of UO 2 by One-and two-electron oxidants, Mater. Res. Soc. Symp. Proc. 807 (2003) 277–282, doi:10.1557/ PROC-807-77.

[20] A. Barreiro Fidalgo, Y. Kumagai, M. Jonsson, The role of surface-bound hydroxyl radicals in the reaction between H2O2 and UO2, J. Coord. Chem. 71 (2018) 1799–1807, doi:10.1080/00958972.2018.1466287.

[21] Y. Kumagai, A. Barreiro Fidalgo, M. Jonsson, Impact of stoichiometry on the mechanism and kinetics of oxidative dissolution of UO2 induced by H2O2 and γ-irradiation, J. Phys. Chem. C 123 (2019) 9919–9925, doi:10.1021/acs.jpcc. 9b00862.

[22] A.C. Maier, E.H. Iglebaek, M. Jonsson, Confirming the formation of hydroxyl radicals in the catalytic decomposition of H2O2 on metal oxides using coumarin as a probe, ChemCatChem 11 (2019) 5435–5438, doi:10.1002/cctc. 201901316.

[23] A.J. Elliot, M.P. Chenier, Radiolysis of 4.5mol dm− 3 LiOH with 6Li (n, α) 3H ion recoil, J. Nucl. Mater. 187 (1992) 230–238, doi:10.1016/0022-3115(92)90502-C.

[24] G.V. Buxton, C.L. Greenstock, W.P. Helman, A.B. Ross, Critical review of rate constants for reactions of hydrated electrons, hydrogen atoms and hydroxyl radicals ($\cdot$ OH/$\cdot$ O− in aqueous solution, J. Phys. Chem. Ref. Data 17 (1988) 513–886, doi:10.1063/1.555805.

[25] S.P. Mezyk, D.M. Bartels, Direct EPR measurement of Arrhenius parameters for the reactions of H· atoms with H 2 O 2 and D· atoms with D 2 O 2 in aqueous solution, J. Chem. Soc., Faraday Trans. 91 (1995) 3127–3132, doi:10.1039/FT9959103127.

[26] A.J. Elliot, G.V. Buxton, Temperature dependence of the reactions OH + O and OH + HO2 in water up to 200℃, J. Chem. Soc., Faraday Trans. 88 (1992) 2465–2470, doi:10.1039/FT9928802465.

[27] Z. Cai, X. Li, Y. Katsumura, O. Urabe, Radiolysis of bicarbonate and carbon-ate aqueous solutions: product analysis and simulation of radiolytic processes, Nucl. Technol. 136 (2001) 231–240, doi:10.13182/NT01-A3241.

[28] J. Smellie, M. Laaksoharju, P. Wikberg, S.E. Äspö, Sweden: a natural ground-water flow model derived from hydrogeochemical observations, J. Hydrol. 172 (1995) 147–169, doi:10.1016/0022-1694(95)02720-A.

[29] P.A. Hong, Y.-.Y. Macauley, Corrosion and leaching of copper tubing exposed to chlorinated drinking water, Water, Air, Soil Pollut 108 (1998) 457–471.

[30] H. Soomro, N. Zainuddin, H. Daud, J. Sunday, N. Jamaludin, A. Abdul-lah, M. Apriyanto, E.A. Kadir, Variable step block hybrid method for stiff chemical kinetics problems, Applied Sciences 12 (2022) 4484, doi:10.3390/ app12094484.

[31] E.A. Celaya, J.A. Aguirrezabala, P. Chatzipantelidis, Implementation of an adap-tive BDF2 formula and comparison with the MATLAB Ode15s, ICCS (2014) 1014–1026, doi:10.1016/j.procs.2014.05.091.

[32] J.A. LaVerne, L. Tandon, H2 production in the radiolysis of water on CeO2 and ZrO2, J. Phys. Chem. B 106 (2002) 380–386, doi:10.1021/jp013098s.

[33] H. Christensen, Calculations simulating spent-fuel leaching experiments, Nucl. Technol. 124 (1998) 165–174, doi:10.13182/NT98-A2916.

[34] A.J. Elliot, D.R. McCracken, Computer modelling of the radiolysis in an aqueous lithium salt blanket: suppression of radiolysis by addition of hydrogen, Fusion Eng. Des. 13 (1990) 21–27, doi:10.1016/0920-3796(90)90028-5.

[35] B. Pastina, J.A. LaVerne, Hydrogen peroxide production in the radiolysis of water with heavy ions, J. Phys. Chem. A 103 (1999) 1592–1597, doi:10.1021/ jp984433o.

[36] H.A. Schwarz, J.M. Caffrey Jr, G. Scholes, Radiolysis of neutral water by cy-clotron produced deuterons and helium Ions1, J. Am. Chem. Soc. 81 (1959) 1801–1809, doi:10.1021/ja01517a008.

[37] J.A. LaVerne, R.H. Schuler, W. Burns, Track effects in radiation chemistry: pro-duction of hydroperoxo radical within the track core in the heavy-particle radi-olysis of water, J. Phys. Chem. 90 (1986) 3238–3242, doi:10.1021/j100405a037.

[38] J.A. LaVerne, The production of OH radicals in the radiolysis of water with ^{4}He ions, Radiat. Res. 118 (1989) 201–210, doi:10.2307/3577437.

[39] J.A. LaVerne, H. Yoshida, Production of the hydrated electron in the radiolysis of water with helium ions, J. Phys. Chem. 97 (1993) 10720–10724, doi:10.1021/ j100143a033.

[40] J.A. LaVerne, S. Pimblott, New mechanism for H2 formation in water, J. Phys. Chem. A 104 (2000) 9820–9822, doi:10.1021/jp002893n.

[41] H. Fricke, S. Morse, The chemical action of roentgen rays on dilute ferrosul-phate solutions as a measure of dose, Am. J. Roentgenol. Radium Therapy Nucl. Med 18 (1927) 430–432.

[42] G. Choppin, J.-.O. Liljenzin, J. Rydberg, C. Ekberg, Chapter 8 - radiation ef-fects on matter, in: Radiochemistry and Nuclear Chemistry (Fourth Edition), Academic Press, Oxford, 2013, pp. 209–237, doi:10.1016/B978-0-12-405897-2. 00008-2.

[43] R. Meesat, S. Sanguanmith, J. Meesungnoen, M. Lepage, A. Khalil, J.-.P. Jay-Gerin, Utilization of the ferrous sulfate (Fricke) dosimeter for evaluating the radioprotective potential of cystamine: experiment and Monte Carlo simula-tion, Radiat. Res. 177 (2012) 813–826, doi:10.1667/RR2829.1.

[44] W. Barb, J. Baxendale, P. George, K. Hargrave, Reactions of ferrous and ferric ions with hydrogen peroxide. Part II.—The ferric ion reaction, Trans. Faraday Soc. 47 (1951) 591–616, doi:10.1039/TF9514700591.

[45] M. Amme, W. Bors, C. Michel, K. Stettmaier, G. Rasmussen, M. Betti, Effects of Fe (II) and hydrogen peroxide interaction upon dissolving UO2 under geologic repository conditions, Environ. Sci. Technol. 39 (2005) 221–229, doi:10.1021/ es040034x.

[46] A. Ogata, R.B. Banks, A Solution of the Differential Equation of Longitudinal Dispersion in Porous media: Fluid Movement in Earth Materials, US Govern-ment Printing Office, 1961.

[47] F. Nielsen, K. Lundahl, M. Jonsson, Simulations of H_2O_2 concentration profiles in the water surrounding spent nuclear fuel, J. Nucl. Mater. 372 (2008) 32–35, doi:10.1016/j.jnucmat.2007.01.279.

[48] P.L. Zanonato, P. Di Bernardo, Z. Szabó, I. Grenthe, Chemical equilibria in the uranyl (VI)–peroxide–carbonate system; identification of precursors for the formation of poly-peroxometallates, Dalton Trans 41 (2012) 11635–11641, doi:10.1039/C2DT31282D.

[49] A. Poulesquen, C. Jegou, Influence of alpha radiolysis of water on UO2 ma-trix alteration: chemical/transport model, Nucl. Technol. 160 (2007) 337–345, doi:10.13182/NT07-A3904.

[50] H. Christensen, Calculation of corrosion rates of alpha-doped UO2, Nucl. Tech-nol. 155 (2006) 358–364, doi:10.13182/NT06-A3768.

[51] J. Cobos, L. Havela, V. Rondinella, J. de Pablo, T. Gouder, J.-.P. Glatz, P. Carbol, Corrosion and dissolution studies of UO2 containing α-emitters, Radiochim. Acta 90 (2002) 597–602, doi:10.1524/ract.2002.90.9-11_2002.597.